The International Journal of Advanced Manufacturing Technology (2020) 107:3581–3592
https://doi.org/10.1007/s00170-020-05295-w

ORIGINAL ARTICLE

# Theoretical and experimental study of temperature field in noncircular high-speed grinding

Tao Liu [1,2] · Zhaohui Deng [1,2] · Lishu Lv [1,2] · Jun Yi [1,2] · Shuailong She [1,2] · Linlin Wan [1,2]

Received: 7 September 2019 / Accepted: 31 March 2020 / Published online: 18 April 2020


## Abstract

A study of a noncircular workpiece grinding mechanism for improving the quality of noncircular grinding was conducted. By combining the principle of heat transfer, the geometry, and the kinematics in the high-speed grinding of noncircular workpiece, a variable heat flow distribution model was developed to evaluate the temperature field. Through a reasonable hypothesis and simplification, a three-dimensional (3D) finite element (FE) simulation model was established based on the variable heat source distribution model. The temperature field in the workpiece was simulated with a 3D transient thermal FE code. The grinding temperature test platform using an infrared thermal imager was established. Experimental results were compared with the results of a simulation; the comparison results showed that the temperature field obtained from ANSYS and the infrared thermal imager were nearly identical, the maximum error was 5.91%, and the simulation results truly reflected noncircular high-speed grinding heat conditions. Based on the analysis of experimental and simulation results, the influence of grinding process parameters on the grinding temperature in high-speed grinding of the noncircular workpiece was revealed. This work should be helpful in solving the problem of thermal damage on the surface of noncircular workpieces during high-speed grinding.

**Keywords** Noncircular workpieces · High-speed grinding · Variable heat flow · Finite element simulation · Infrared thermal imager

## Nomenclature

| | |
|---|---|
| $v_t$ | The resultant relative velocity between the grinding wheel and the workpiece (m $s^{-1}$) |
| $v_f$ | The infeed velocity (m $s^{-1}$) |
| $v_w$ | The relative velocity of workpiece (m $s^{-1}$) |
| $\omega$ | the angular velocity(rad/s) |
| $\theta$ | The angle of the contact entry point (rad) |
| $\varphi$ | The workpiece rotational angles (rad) |
| $M'_w$ | The specific material removal rate |
| $V$ | The volume of removed material($mm^3$) |
| $r_w$ | The radius of curvature of the workpiece (mm) |
| $l_c$ | The length of contact arc (mm) |
| $\xi$ | The angle between the starting point and arbitrary point on the grinding arc area |
| $x_i$ | Location of any point i in positive x direction (mm) |
| $r_s$ | The radius of grinding wheel (mm) |
| $v_s$ | The grinding wheel speed (m $s^{-1}$) |
| $n_w$ | The workpiece speed (rad $min^{-1}$) |
| $a_p$ | The grinding depth (mm) |
| $b$ | The grinding width (mm) |
| $q_w$ | The average heat flux into the workpiece (W $m^{-2}$) |
| $q_t$ | The total heat flux in grinding contact zone (W $m^{-2}$) |
| $q_s$ | The heat flux density into the grinding wheel (W $m^{-2}$) |
| $q_c$ | heat flux due to convection (W $m^{-2}$) |
| $P$ | The net grinding power (W) |
| $R_w$ | The heat partition ratio to the workpiece (Dimensionless) |
| $\beta_w$ | The thermal contact coefficient of workpiece material (W $m^{-2}$ $K^{-1}$) |
| $k_w$ | The thermal conductivity of workpiece material (W $m^{-1}$ $K^{-1}$) |
| $k_g$ | The abrasive thermal conductivity (W $m^{-1}$ $K^{-1}$) |
| $\rho_w$ | The material density t of workpiece (kg $m^{-3}$) |
| $c_w$ | The specific heat capacity of the workpiece material (J $kg^{-1}$ $K^{-1}$) |
| $h$ | The heat transfer coefficient (W $m^{-2}$ $K^{-1}$) |
| $r_0$ | The effective contact radius of abrasive particles (mm) |

✉ Zhaohui Deng
edeng0080@vip.sina.com

[1] Hunan Provincial Key Laboratory of High Efficiency and Precision Machining of Difficult to Machine Material, Hunan University of Science and Technology, Xiangtan 411201, Hunan, China

[2] Intelligent Manufacturing Institute, Hunan University of Science and Technology, Xiangtan 411201, Hunan, China

$Q_{GR}$ The Real-time power of grinding (W)
$Q_{EM}$ The idle power of grinder (W)
$Q_t$ The heating power of heat source (W)
$T_m$ The measured temperature (°C)
$T_s$ The Simulation temperature (°C)
$T_\infty$ The ambient temperature(°C)

## 1 Introduction

Noncircular workpieces are extensively used as key components in many industrial fields, such as camshafts and oval-section pistons. Their machining quality plays a critical role in the motion control accuracy and durability of engines in the automotive industry [1]. In addition, for noncircular grinding and mass production, it is far from easy to guarantee high grinding quality and high processing efficiency simultaneously [2, 3]. In recent years, with the wide use of cubic boron nitride (CBN) wheels, high-speed grinding shows great advantages in improving quality and efficiency [4], and the workpiece material is machined by more grains which will lead to a smaller force, less wheel wear, better surface quality [5], which can further improve the machine efficiency dramatically. However, most of these focus on infeed or effective depth of cut [6] and do not consider the thermal damage caused by the high temperature, such as surface burn, over-tempering, residual tensile stresses, cracking, and rehardening.

Therefore, theoretical investigation of grinding temperature field is required, as stated by Malkin [7]. A model was created for the dry grinding of ferrous materials by Guo [8, 9], which has been successful for shallow grinding. Later, a partition ratio model was created by Rowe [10], which could be used to calculate the temperature in the shallow or deep grinding of different workpiece materials and grinding wheels. Jiang and Ge [11] created an integrated model of the surface grinding process while considering the complicated microscopic interactions between grains and workpiece material in the grinding contact zone, and experimental results demonstrated that the model was in good accordance under dry and wet grinding conditions. The heat load is regarded as a consecutive heat source moving at the workpiece velocity. The thermal analysis mainly requires knowledge of the form of the heat source (parabola distribution [12], triangle distribution [13], the Rayleigh distribution [14]), the temperature right round the grinding zone (by the thermocouple [15], thermal infrared imager [16]), the actual contact length [17], and so on.

Many examinations of the thermal effects in grinding have been conducted both analytically and numerically. Numerical simulation of the grinding process increased significantly as the development of computer technology [18]. Researchers had more powerful and affordable method to predict workpiece temperatures by implementing numerical models without having to carry out many tedious experiments [19]. Li [20] created a stochastically grain-discretized model that considered grain-workpiece micro interactions (i.e., rubbing, plowing, and cutting) and was successful for 2D/3D temperature mapping prediction in surface grinding. Nguyen et al. [21, 22] developed temperature-dependent finite element heat transfer model to describe the temperature field of traverse cylindrical grinding and plunge cylindrical grinding process.

Furthermore, for the grinding temperature in noncircular grinding, few studies have been conducted [23]. In addition, a thorough understanding of the kinematic relationships in the high-speed grinding of noncircular workpieces is necessary. Once this is obtained, a heat model based on the geometric model can be used to predict grinding temperatures, which is a help to reveal the evolution law of grinding thermal in noncircular grinding.

This study was concerned with the high-speed grinding of noncircular workpieces in various applications. The main research content was as follows: (1) with the investigation of generalized models of geometry and kinematics for high-speed grinding of arbitrarily shaped noncircular workpieces, a variable heat flow distribution model for noncircular high-speed grinding that considers instantaneous variations of the geometric, kinematic, and specific grinding energy in the workpiece was established; (2) numerical simulations were developed to calculate the temperature distribution in the workpiece during noncircular cylindrical grinding; (3) grinding experiments were performed by using an infrared system to measure the grinding temperature for validating the analytical and numerical model.

## 2 Model description

### 2.1 Geometry and kinematics of noncircular peripheral grinding

The geometry and kinematics of generalized noncircular peripheral grinding are illustrated in Fig. 1. The speed of the grinding wheel and the workpiece rotating, wheel infeeding, and radial retracting generate an arbitrary noncircular profile on the workpiece. For the sake of simplicity, it is assumed that the grinding wheel is regarded as a relative movement around a fixed noncircular workpiece in the deduce of the grinding kinematics [24]. The workpiece rotational angle φ represents the fundamental independent argument used to the grinding process modeling. In the actual grinding scenario, ω(φ) is the angular velocity of the noncircular workpiece. The infeed speed of grinding wheel $v_f(\varphi)$ and the relative speed of workpiece $v_w(\varphi)$, as well as the resultant relative velocity $v_t(\varphi)$

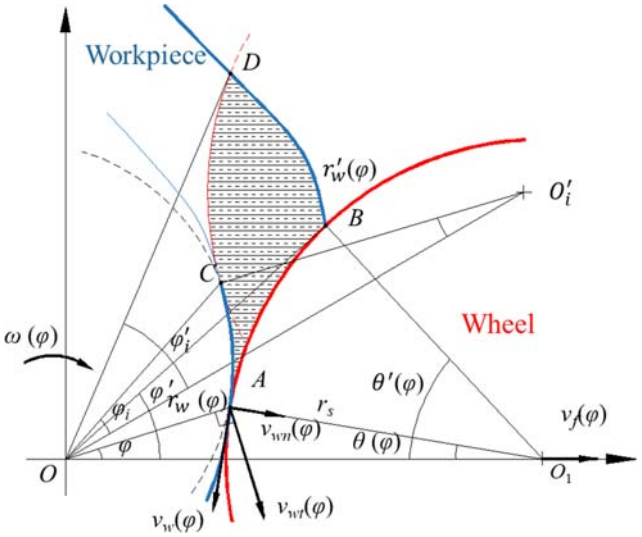


**Fig. 1** Kinematics and geometry of noncircular grinding

between the wheel and the workpiece are given with the angle φ. The relationships as follow:

$$\begin{cases} v_w(\varphi) = \omega(\varphi) r_w(\varphi) \\ v_f(\varphi) = \dfrac{v_w(\varphi)\sin(\varphi + \theta(\varphi))}{\cos\theta(\varphi)} \\ v_t(\varphi) = \dfrac{v_w(\varphi)(\cos(\varphi + \theta(\varphi))\cos\theta - \sin(\varphi + \theta(\varphi))\sin\theta(\varphi))}{\cos\theta(\varphi)} \end{cases} \tag{1}$$

$$\theta(\varphi) = \arcsin\frac{r_w(\varphi) sin\varphi}{r_s} \tag{2}$$

All velocities vary with respect to φ during rotation of the workpiece because of the vary geometry: (1) the distance between the center of grinding wheel and the rotation center of noncircular workpiece $OO_1$, and (2) the angle of the cut-in point θ(φ) and the radius of curvature $r_w(\varphi)$ are continuously changing. The contact length $l_c(\varphi)$ also varies at each instant of workpiece rotation, which is correspondent to the difference between the angle of the cut-in point θ(φ) and the angle of the cut-out point θ′(φ). The deformations of the wheel and the workpiece is neglected, so $l_c(\varphi)$ is given as [24]:

$$\begin{aligned} l_c(\varphi) &= r_s\left(\theta'(\varphi) - \theta(\varphi)\right) \\ &= \left(1 \pm \frac{v_w}{v_s}\right)\sqrt{2\frac{r_w(\varphi)\, r_s}{r_w(\varphi) + r_s} a_p} \end{aligned} \tag{3}$$

where $r_s$ is the radius of the grinding wheel.

The specific material removal rate $M'_w(\varphi)$ is the other significant output of the geometrical and kinematic model, which is further used as a pivotal parameter in the heat model. The calculation of the specific material removal rate variation, $M'_w(\varphi)$, is based on the derivative of volume of the removed material $V$ with respect to time:

$$M'_w(\varphi) = \frac{dV}{dt}(\varphi) = \frac{\partial V}{\partial \varphi}\frac{\partial \varphi}{\partial t} = \frac{\partial V}{\partial \varphi}\frac{v_w(\varphi)}{2\pi r_w(\varphi)} \tag{4}$$

where

$$V(\varphi) = b\left(\int_{\angle AOB}^{\angle AOD}\frac{1}{2}r_1^2(\varphi)d\varphi - \int_{\angle AOB}^{\angle AOD}\frac{1}{2}r_0^2(\varphi)d\varphi - \int_{\angle AOB}^{\angle COD}\frac{1}{2}r_c^2(\varphi)d\varphi\right) \tag{5}$$

From Fig.1 A and B, respectively, are the cut-in point and the cut-out point with the workpiece rotational angle φ, and C and D, respectively, are the cut-in point and the cut-out point with the workpiece rotational angle $\varphi_i$. $r_0$ is the radius of curvature of the workpiece contour in the contact cut-in point, $r_1$ is the radial distance of the contact cut-out point, $r_c$ is the radial distance along the contact zone, and $b$ is the grinding width.

In cylindrical grinding, it should be noted that both $l_c(\varphi)$ and $M'_w(\varphi)$ are constant [25]. In contrast, because of the discontinuous form movement of the noncircular contour, the specific material removal rate and contact length are dynamically changed, finally, results in modification of the grinding temperature, and it can even cause thermal damage.

## 2.2 Thermal model of noncircular peripheral grinding

Hitherto, many heat flow distribution models have been proposed based on surface grinding, such as the triangle distribution heat source model and rectangular heat source model. However, it is far more complicated for the situation of noncircular grinding, and the temperature field distribution is significantly different from the other grinding ways because the contact length and the specific material removal rate change throughout the rotation of the workpiece, and the heat flow into the workpiece and the specific energy also vary with changes in both $l_c(\varphi)$ and $M'_w(\varphi)$.

The quadratic curve heat flow model was assumed based on the special chip in the process and abrasive dust thickness changes in cylindrical grinding, and it could accurately predict the high-speed cylindrical grinding temperature [26]. Noncircular peripheral grinding can be regarded as the stack of countless cylindrical grinding. According to the geometry and kinematics of noncircular grinding, it was assumed that the actual heat flow into the workpiece during noncircular grinding also presents a conic distribution. Therefore, a new heat flux distribution model (see Fig.2) which is similar to the curve profile was developed to calculate the temperature and energy partition ratio in the noncircular grinding.

As in Ref. [26], a quadratic distribution was described as:

$$q(x_i) = q_w\left(-\frac{6}{l_c^2}x_i^2 + \frac{6}{l_c}x_i\right) \tag{6}$$

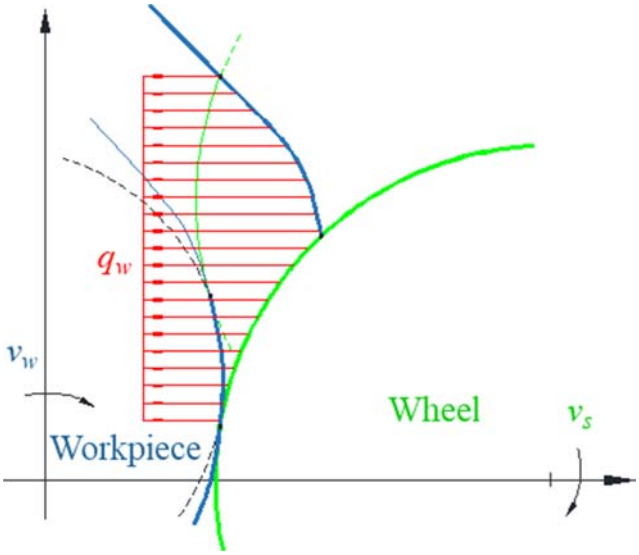


**Fig. 2** Realistic heat flux to the workpiece in the noncircular grinding

$x_i$ is shown in polar coordinates:

$$x_i = r_w(\varphi)\sin\xi \tag{7}$$

Substituting Eqs. (3) and (9) into Eq. (8), the function of the heat source distribution in the form of polar coordinates is as follows:

$$q(\varphi,\theta_i) = q_w\left(-\frac{3(r_w(\varphi)+r_s)r_w(\varphi)}{r_s a_p}\sin^2\xi + 6\sqrt{2\frac{r_w(\varphi)(r_w(\varphi)+r_s)}{r_s a_p}}\sin\xi\right) \tag{8}$$

Here, ξ is the angle between the starting point and arbitrary point on the grinding arc area, and $q_w$ is the heat flow into the workpiece and can be expressed as.

$$q_w = q_t R_{ws} = \frac{P}{bl_c}R_{ws} = \frac{P}{b\left(1\pm\frac{v_w}{v_s}\right)\sqrt{2\frac{r_w(\varphi)\,r_s}{r_w(\varphi)+r_s}a_p}}R_{ws} \tag{9}$$

where $P = F_t \times v_s$, which is relevant with the specific material removal rate variation $M_w'(\varphi)$, and $R_{ws}$ is the heat partition ratio between the workpiece and the grinding wheel. It is seen that the heat flow varies with the radius of curvature $r_w$, while $r_w$ varies with the workpiece rotational angles φ. So, the heat source distribution is variable with the workpiece rotational angles.

Many scholars have performed extensive research on the heat partition ratio of grinding, and they have proposed many theoretical models for different grinding conditions [27]. However, the actual grinding process is complicated, and the heat partition ratio to the workpiece $R_w$ is a variable. It is related to grinding wheel's line speed $v_s$, workpiece speed $n_w$, grinding depth $a_p$, material properties ($k$, ρ, $c$), and so on. The previous theoretical models were established in a certain hypothesis to simplify the modeling process and cannot completely reflect the actual grinding situation, especially for more complex grinding process of noncircular contour parts. In the situation here, based on the previous research, a more straightforward approach to determine the heat partition ratio in the workpiece was used.

Unlike the previous method to calculate the heat partition ratio based on the theoretical analysis, a method is presented here to determine the heat partition ratio based on the surface temperature of the workpiece measured during the grinding experiment in combination with that obtained by numerical calculation. As shown in Fig. 3, $Q_{GR}$ and $Q_{EM}$ are the grinding power and the idle power of the grinder, respectively, which can be measured by a digital power meter. The thermal partition ratio $R_w$ is estimated according to the existing theoretical model of grinding heat partition. Based on the variable heat source model and theoretical heat partition ratio, the predicted grinding temperature is determined by finite element (FE) simulation. By fitting measured temperatures to the predicted response using FE simulation, the actual heat partition ratio of the workpiece is determined.

In this research, henceforth, an automobile camshaft is used as a typical noncircular workpiece to study the grinding temperature.

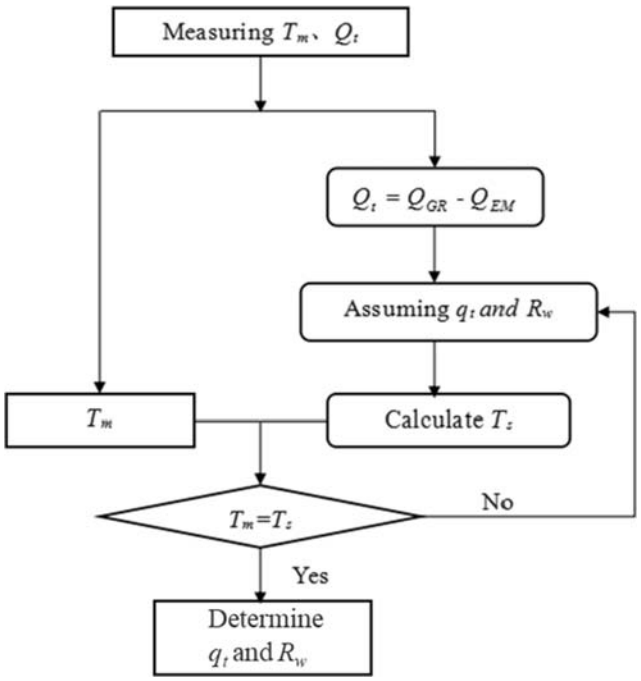


**Fig. 3** Calculation procedure of heat partition ratio

## 3 Numerical simulation of temperature in noncircular high-speed grinding

### 3.1 Process of the numerical simulation

Three-dimensional, multi-step transient thermal models were established by the FE software ANSYS 15. Figure 4 illustrates the schematic diagram of heat transfer during the grinding of a camshaft. The temperature field of the entire workpiece was calculated based on an unsteady state heat conduction equation, which is the basis of finite element simulation of heat transfer.

$$\frac{\partial}{\partial x}\left(k_{xx}\frac{\partial T}{\partial x}\right)+\frac{\partial}{\partial y}\left(k_{yy}\frac{\partial T}{\partial y}\right)+\frac{\partial}{\partial z}\left(k_{zz}\frac{\partial T}{\partial z}\right)+\dot{\dot{q}} = \rho c\frac{dT}{dt} \tag{10}$$

in which $q$ is the heat rate per unit volume generated, where ρ is the density of the workpiece and c is the specific heat, and $k$ is the thermal conductivity. The camshaft was made of chilled cast iron, and the material properties are listed in Table 1.

It is necessary to make some assumptions and simplifications for the heat transfer model on the basis of the actual grinding conditions to improve the accuracy of the simulation. Therefore, in addition to the basic assumptions, the following assumptions and simplifications were made for the simulation model of the high-speed grinding of camshafts:

(1) When the simulation model was established, the abrasion of the grinding wheel and the phase change of the camshaft material were not considered;

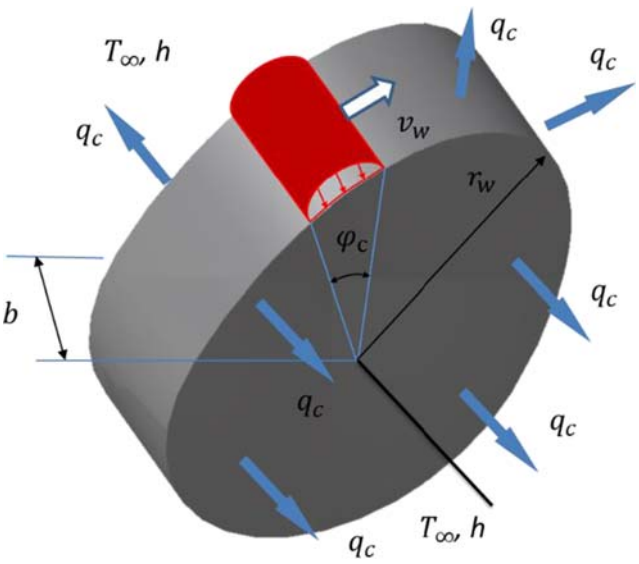


**Fig. 4** Conduction in the workpiece during noncircular high-speed grinding

(2) Because the grinding experiment used the dry-grinding method, the cam surface and the surrounding environment of heat convection were negligible.

A 3D thermal solid element Solid 90 was selected for transient nonlinear thermal analysis, and which is suitable for describing curved boundaries. Through a comparative simulation of the three different unit specifications (0.01, 0.05, and 0.1 mm), it was found that the difference of calculation results from 0.1 to 0.01 mm was less than 5%, but the calculation time greatly increased. Therefore, the mesh was divided according to the unit size of 0.05 mm.

In the grinding process, the cutting fluid is difficult to enter contact area of wheel-workpiece. Some researchers have demonstrated that the heat transfer mechanism of the dry-grinding process is similar to the actual grinding [12, 16, 28]. So this study mainly focused on the dry-grinding process of the camshaft, without considering the heat taken away by the grinding fluid, and the heat take away by the abrasive chip thickness was neglected, i.e., heat flux due to convection $q_c = 0$. The ambient temperature $T_\infty$ is set as 25 °C according to the actual experimental circumstances, $h$ is the heat transfer coefficient. Therefore, the energy distribution relation of the contact region is as follows.

$$q_t = q_w + q_s \tag{11}$$

where $q_s$ is the heat flux density that flows into the grinding wheel, according to previous work [17]. Thus,

$$R_{ws} = \frac{q_w}{q_w + q_s} = \left[1 + \frac{0.974k_g}{\beta_w\sqrt{r_0 v_s}}\right]^{-1} \tag{12}$$

Therefore, $q_w$ can be expressed by the following formula:

$$q_w = \left[1 + \frac{0.974k_g}{\beta_w\sqrt{r_0 v_s}}\right]^{-1} \cdot \frac{P}{l_c \cdot b} \tag{13}$$

Here, $\beta_w$ is the thermal contact coefficient of the workpiece material, $k_w$ is the thermal conductivity of the workpiece material, $\rho_w$ is the workpiece material density, $c_w$ is the specific heat capacity of the workpiece material, and $k_g$ is the abrasive thermal conductivity. For CBN wheels, $k_g = 240$ W m$^{-1}$ k$^{-1}$, and $r_0$ is the effective contact radius of the abrasive particles. Typical calculation values were adopted in this study, $r_0 =$ 15 μm.

According to the heat flux models obtained by the above calculation, the simulations of grinding temperature were performed. According to the calculation process shown in Fig. 3, the true heat flux of the workpiece was continuously corrected. As in the grinding process, the time to change the workpiece surface temperature distribution also showed significant changes, so transient thermal analysis was chosen. The heat flux with the change in time imposed was constantly

**Table 1** Material properties of chilled cast iron

| Workpiece | Density ρ (kg $m^3$) | Thermal conductivity $k$ (W $m^{-1}$ $k^{-1}$) | Specific heat capacity $c$ (J $kg^{-1}$ $K^{-1}$) |
|---|---|---|---|
| Chilled cast iron | 7220 | 50.24 | 460 |

varying, so the time step and load step types needed to be defined, and each step was divided into several substeps.

In the process of camshaft grinding, the direction and size of the heat flux changed with the grinding process. It was essential to select the appropriate coordinates to achieve the loading of the heat source for the simulation of the grinding temperature. According to the characteristics of the cam-grinding process, each load step heat source was turned by 1°, and the time of each load step was determined by the rotation speed of the cam. The cam contour surface was subjected to multiple segmentation processing according to the actual grinding conditions, and the corresponding relation of grinding area with time was established. The grinding arc was substituted for its secant line, the heat flux was projected to the coordinates for the direction of the secant, and the load along the direction of the coordinate values on the corresponding moment was acquired by calculation. The load value and loading direction of the heat flux change over the direction of the tangent line of the grinding arc. The ratio between the actual load value and the calculated theoretical value should be taken as the correction coefficient, which was used to correct the load value on the coordinate axis, and the loading load at the previous time should be deleted and then reloaded with the modified value to guarantee the correct loading of thermal load. This step was repeated until all time steps were completed.

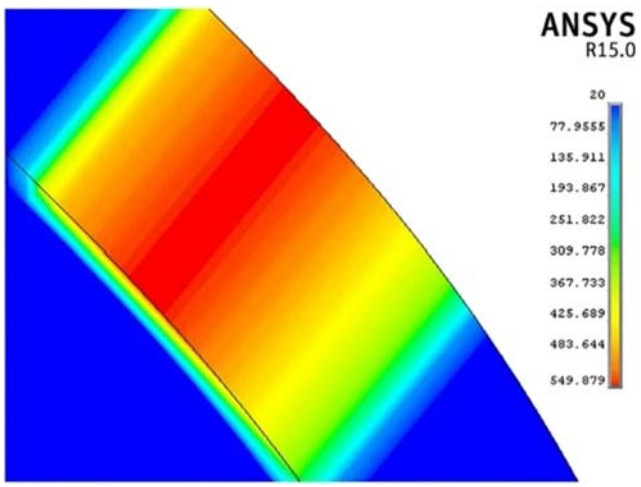


**Fig. 5** Temperature field distribution on camshaft surface

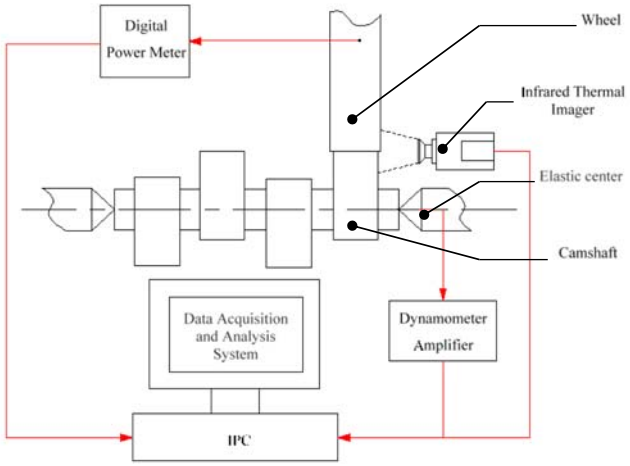


**Fig. 6** Schematic diagram of workpiece surface temperature measurement device

### 3.2 Results of the simulation

The temperature profile of the grinding process can be obtained by using the universal postprocessor (POST1). According to the analysis of the last section, most of the grinding heat enters the workpiece, which leads to the increase in the surface temperature of the cam. Because variety of the heat source in the cam contour surface, the grinding temperature is also constantly changing, resulting in the workpiece undergoing different time-temperature changes. The grinding temperature distribution of the cam is shown in Fig.5, where the workpiece speed $n_w = 90$ r/min, wheel line speed $v_s = 120$ m/s, and grinding depth $a_p = 0.01$ mm. According to the simulation results, it is found that the heat source increased firstly and then decreased from cut-in to cut-out; the temperature field is not completely symmetrical along the length of the contact arc.

## 4 Experimental validation

### 4.1 Experimental apparatus

High-speed grinding experiments of camshaft were performed on a grinding-temperature-measuring platform to verify the theoretical and numerical models. The platform was mainly composed of a super high-speed camshaft compound grinding machine, infrared thermal imager, data acquisition system, digital power meter, and other components, as shown in Fig. 6. The maximum speed of the ultra high-speed camshaft CNC compound grinding machine can reach 10,000 r/min. The grinding machine uses a vitrified bond CBN grinding wheel whose particle size is 70#, radius of grinding wheel is 200 mm, width of grinding wheel is 25 mm, and maximum speed of grinding wheel is 200 m/s, and a diamond wheel is used for dressing the grinding wheel. The digital power meter uses the WT330 series power analyzer produced by Yokota,

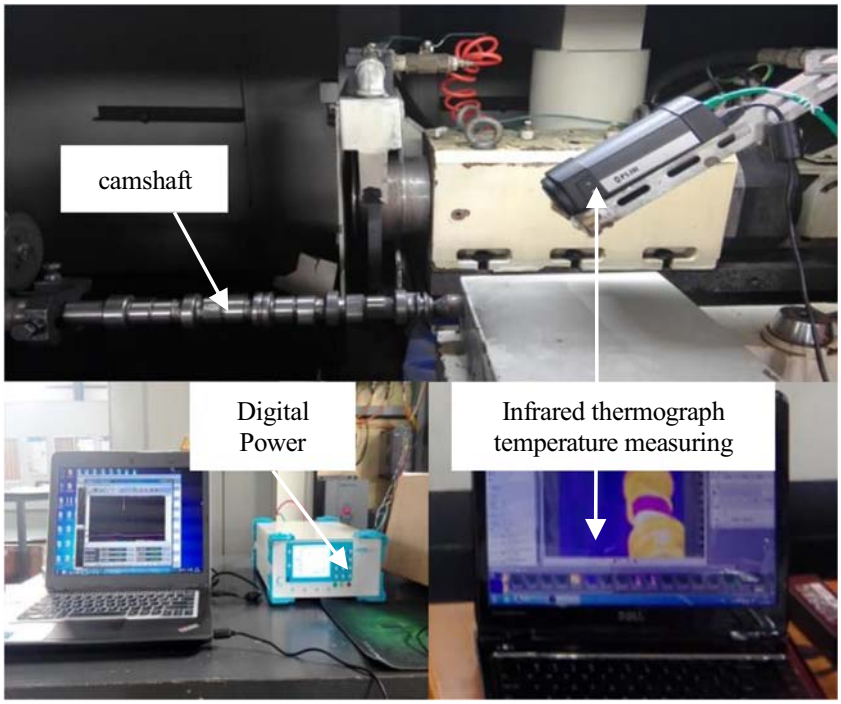


**Fig. 7** Photographs of grinding temperature experiment

Japan. The sampling frequency is 0.1 s, which was used to measure the power of the spindle system.

As a typical noncircular workpiece, and the camshaft workpiece curvature radius and surface grinding temperature gradient are large, the thermocouple thermometry makes it difficult to measure to the temperature of whole workpiece surface. Thermal imaging technology is widely used in grinding temperature measurement; many literatures have reported its advantages in measuring grinding area temperature [16]. Therefore, an infrared thermal imager was conducted using to temperature measurements. While the cutting fluid has the negative influence on the infrared thermal imager, therefore the dry-grinding process was conducted. To calibrate the infrared camera, a miniature black body was used before each experiment. The in-process grinding temperatures were measured through an FLIR SC300 Series infrared video camera, and the frame rate is 60 Hz. The infrared thermal imager was set to a measurement range of 20 to 1200 °C with an accuracy of ± 2 °C and was fitted with a 50-mm focal length germanium lens with a 6.35-mm extension tube. The camera was fixed with respect to the grinding zone, and the data were then sent to a data acquisition computer for analysis.

**Table 2** Grinding test conditions

| Project | Parameter |
|---|---|
| Grinding ways | Dry grinding |
| Grinding wheel | φ400 × 25 mm, CBN |
| Camshaft specimen | Chilled cast iron |
| Infrared thermal imager | − 20 to 1200 °C |
| Grinding wheel speed, $v_s$ | 60, 90, 120, 130, 140, 150 m/s |
| Workpiece speed, $n_w$ | 60, 90, 120, 150 r/min |
| Grinding depth, $a_p$ | 0.005, 0.010, 0.015, 0.020 mm |

## 4.2 Determination of experimental conditions

The contact of the grinding wheel with the workpiece during the grinding of the camshaft can be regarded as a line contact, the contact in the axial direction is uniform, and the grinding process at the center of the workpiece is substantially the same as at the edge position. The coolant concentrate had a negligible cooling effect in the grinding contact regions. And the heat exchange occurred between the edge region and the air relative to the central region is negligible. It can be considered that the temperature of the contact between the cam and the side surface of the wheel was equivalent to the temperature of the entire line contact arc, i.e., the measured temperature by the infrared thermal imager was the temperature of grinding contact zone. According to the experimental scheme, the experimental research was conducted as shown in Fig. 7.

To contain the starting conditions of the experiment were consistent. The seventh piece of camshaft (the best area measured by the infrared thermograph) was machined to the same size; each group of experiment were conducted 3 times, each grinding 5 laps and the highest temperature of the workpiece surface take the arithmetic mean of 3 times of experiments.

Grinding wheel dressing was performed five times per machining [29]. Test conditions are shown in Table 2.

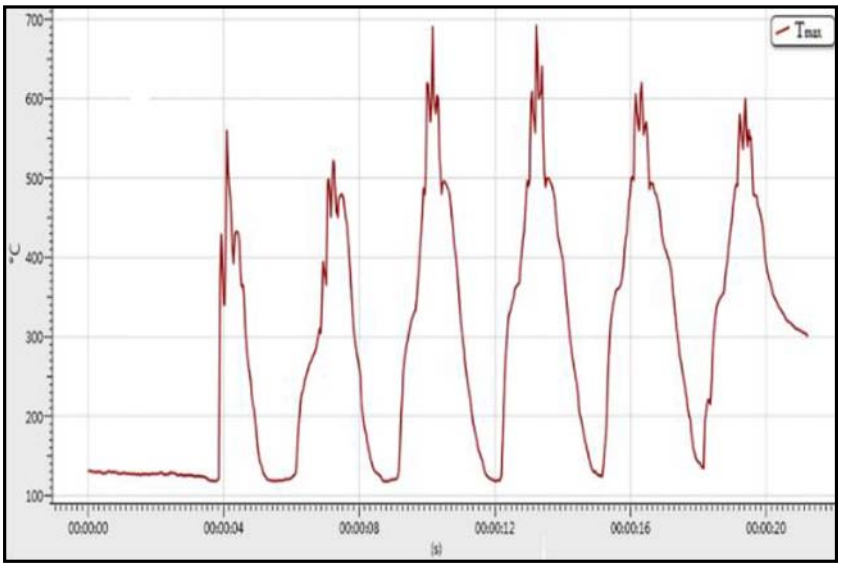


**Fig. 8** The surface maximum temperature curve

## 5 Results and discussion

The results in this work were used to validate the variable heat source distribution model and the numerically predicted temperatures with the experimentally acquired temperatures and to reveal the influence of grinding process parameters on the grinding temperature.

### 5.1 Comparison of simulation value and experimental value under different contour angles

The surface maximum temperature curve when the grinding condition is $v_s = 120$ m/s, $n_w = 90$ r/min, and $a_p = 0.010$ mm is shown in Fig. 8. The measured temperature in the first and second laps was significantly lower, and the value was not stable until the third lap. In the process of grinding, the grinding wheel showed elastic yielding phenomenon. The actual depth of grinding was less than the set of depth grinding, so the temperature of grinding could not reach a stable value. As the grinding increased, the elastic yielding reached the limit value, and the actual depth of grinding was approximately equal to the set depth of grinding. The grinding condition was basically stable in the third and fourth laps, which can be regarded as an ideal collection interval for the grinding temperature.

The simulation of the third section was conducted under idealized conditions, ignoring the size effect of the grinding thickness, the abrasion of the grinding wheel during grinding, and the phase change of the camshaft material; and the cam surface and the surrounding environment of heat convection and debris removed the heat. In the actual grinding process, these neglected factors have a certain impact on the grinding temperature. Therefore, in this section, the experimental results are compared with the simulation results to verify the accuracy of each and to obtain some common conclusions with regularity.

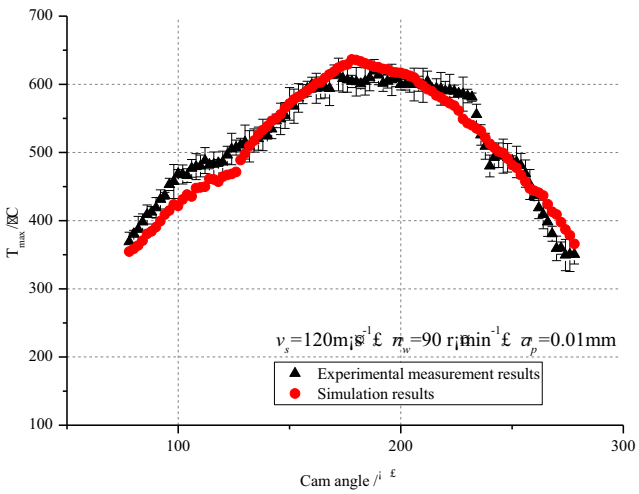


**Fig. 9** Comparison of results of experiment and simulation

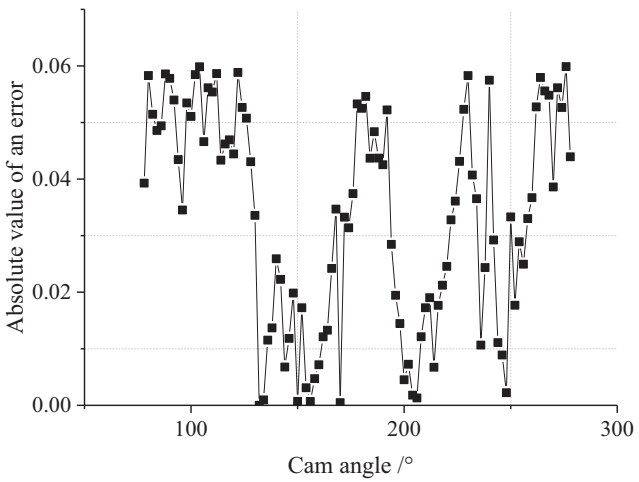


**Fig. 10** Error analysis of experiment and simulation

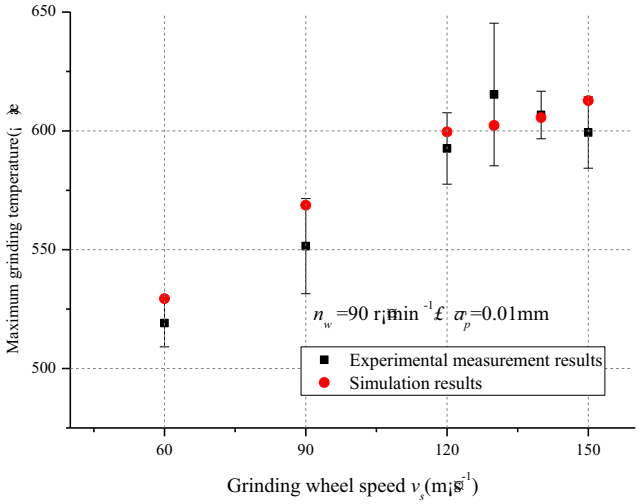


**Fig. 11** Results comparison of experiment and simulation with different grinding speeds

The temperature curve between the simulated values of the cam grinding temperature and the measured values under the dry-grinding condition reflects the deviation between the simulation and the experimental results. With the grinding wheel speed $v_s$ = 120 m/s, workpiece speed $n_w$ = 90 r/min, and grinding depth $a_p$ = 0.010 mm, the grinding temperature curve of the cam and the corresponding simulation results curve are shown in Fig. 8, where the measured values of the third rotation were chosen to comparative analysis with the simulated values.

Figure 9 shows that the simulated temperature curve has smoother abrupt transitions compared with those of the experimental measured temperature curve. In the actual experiment, the response of grinding carriage was lagging, and overcutting or undercut appeared, while the highest temperature of the workpiece surface appeared more easily in the top circle on both sides of the grinding area.

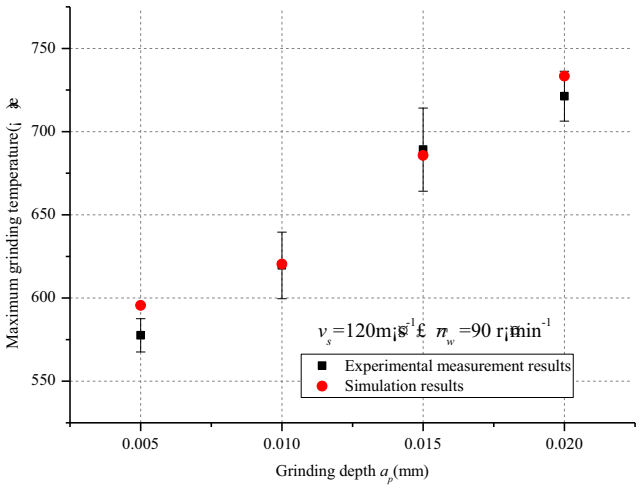


**Fig. 12** Results comparison of experiment and simulation with different grinding depths

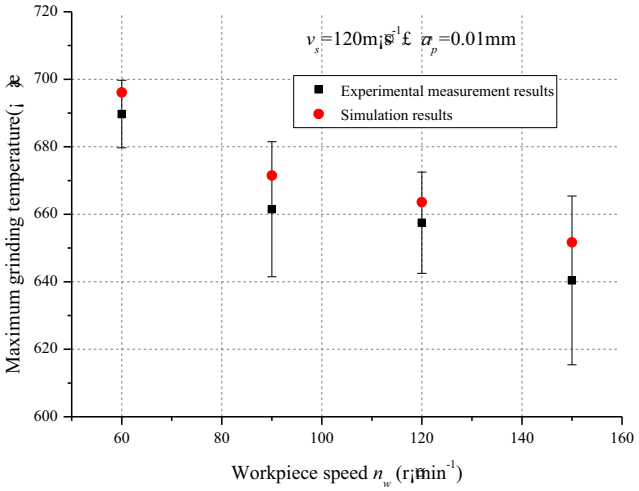


**Fig. 13** Results comparison of experiment and simulation with different workpiece speeds

Because the experiments were based on the grinding method with constant linear speed and the specific material removal rate was related to the curvature radius of each grinding point, and when the linear velocity of the grinding point remained constant, the material removal increased with the curvature radius of each grinding point, both the measured values and the simulated values increased with the increase in the cam lift. Meanwhile, the rotating speed of the grinding point would decrease with the increase in the radius of curvature. Therefore, the grinding temperature increased with the increase in the radius of curvature.

Figure 10 shows that the maximum error between the average value of measured results and the simulation results is 5.91%. The experimental values and the simulated values of the cam surface temperature under the dry-grinding process were basically consistent, which indicates that the simulation results of the heat source distribution model presented in this work are true and reliable.

## 5.2 Comparison of simulation value and experimental value under different grinding parameters

To verify the correctness of the simulation results, the measured values and simulation values of the maximum grinding temperature of the camshaft surface under different grinding parameters were compared and analyzed as shown in Figs. 11, 12, and 13.

By comparing the experimental values and numerical simulation values of the maximum grinding temperature of the cam surface under different grinding parameters, it was found that the simulation value was close to the measured value under different grinding parameters. Therefore, the numerical simulation in Section 3 can be used to calculate the noncircular high-speed grinding process grinding temperature.

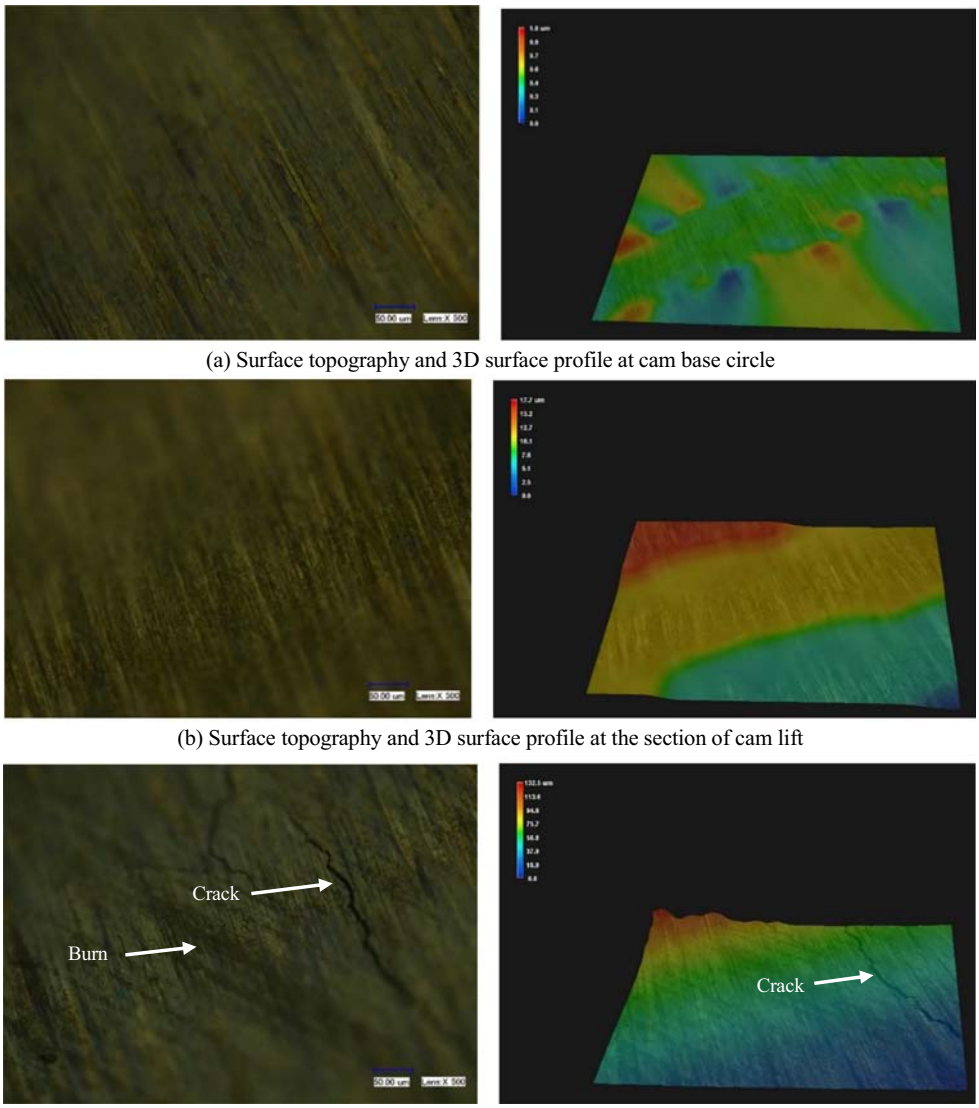


(a) Surface topography and 3D surface profile at cam base circle

(b) Surface topography and 3D surface profile at the section of cam lift

(c) Surface topography and 3D surface profile at top point of cam

**Fig. 14** Surface topography and 3D surface profile image of each part of the cam after grinding

The measured temperature in Fig. 11 increases with the increase in the grinding wheel speed in the range of 60 m/s $< v_s <$ 130 m/s, while it decreases with the increase in the grinding wheel speed in the range of 130 m/s $< v_s <$ 150 m/s, and the temperature is maximizing when $v_s$ = 130 m/s. This is because, the grinding power increases with the increase of the linear velocity of grinding wheel [30]; vibration frequency of process system when $v_s$ is ranged from 130 to 140 m/s is close to the first mode of machine tool, therefore the machine tool vibration is increasing and causes the mutations of grinding force because of the regenerative effect, so the maximum temperature occurs at $v_s$ of 130 m/s. On the other hand, the heat taken away by the high-speed rotating grinding wheel increases; the grinding temperature shows a downward trend compared with the highest temperature point, while the trend that the grinding temperature increasing with the increase of $v_s$ has not changed.

## 5.3 Surface quality with different curvatures

In the grinding process, the grinding zone can be maintained at a normal low temperature when the heat flux density, which is determined by the grinding condition, and is below the critical value of the heat flux of the cooling medium. However, when the grinding heat flux density exceeds the critical value, the temperature of the workpiece surface gradually rises to a thermal equilibrium temperature; then, the high temperature in the grinding zone gradually expands to the low-end zone and keeps growing, and serious burn may lead to the initiation of cracking.

A morphology picture of the ground surface is often examined to detect grinding burn. The surface topography and 3D surface profile images of the base circle, the lift section, and tip circle of the cam after grinding are presented in Fig. 14. There a serious burn with the initiation of cracking occurred

on the top point of cam, while no burn was generated on the base circle of the cam. The grinding burn may occur much more easily on the top point of cam than the base circle of the cam. This is different from ordinary cylindrical grinding. The cam contour surface was composed of multiple surfaces with different curvatures, and the grinding material removal was related to the radius of curvature in different parts of the cam. When constant linear velocity grinding was used in the camshaft grinding, the grinding material removal is proportional to the radius of curvature. Meanwhile, the grinding point rotational speed decreased with the increase in curvature radius. This resulted in a longer valid time of the heat source acting on the grinding point-centered area.

## 6 Conclusions

In this paper, theoretical investigation on temperature field in the high-speed noncircular grinding was conduct. A camshaft as a typical case, the numerical simulation and experimental research on the high-speed grinding temperature under different process parameters were carried out. Thus, the following conclusions are drawn:

- The geometric and kinematic characteristics of noncircular grinding were analyzed, and a variable heat source model was established for the simulation of the grinding temperature of noncircular rotation parts based on variable grinding contact arc length and specific material removal rate.
- Based on the variable heat source model, the FE simulation of the grinding temperature was conducted with the camshaft as a typical noncircular part. According to the simulation results, it is found that the temperature field increased firstly and then decreased from cut-in to cut-out, and it is not completely symmetrical along the length of the contact arc.
- The experiments in the high-speed grinding of camshaft under different process parameters were conducted, the results were compared with the simulation results to verify the proposed model and method, where the maximum error between the measured results and the simulation results was 5.91%, and the variable heat source model was found to be viable. The simulation model provides a theoretical basis for solving the heat damage problem of a noncircular grinding.
- The results of experiment and simulation demonstrated that the grinding temperature increased with the increase in the grinding wheel linear speed and the grinding depth, and it decreased with the increase in the workpiece rotation speed. The grinding burn may occur much more easily on the top point of camshaft.

In future work, the appropriate temperature measuring equipment will be developed to measure grinding temperature under the high-speed noncircular grinding process with cutting fluid. Moreover, the selection of grinding fluid, cooling nozzle, injection pressure, and injection position were studied to reduce grinding thermal damage.

**Funding information** This research was financially supported by the Natural Science Foundation of Hunan province (Grant No. 2017JJ4007), National Natural Science Foundation of China (Grant No. U1809221), and Hunan Provincial Innovation Foundation For Postgraduate (Grant No. CX20190792).

## References

1. Tang H, Deng ZH, Guo YS, Qian J, Reynaerts D (2014) Research on constant grinding depth model for cam grinding. Int J Adv Manuf Technol 74(1–4):351–359
2. Oliveira JFGD, Silva EJD, Guo C, Hashimoto F (2009) Industrial challenges in grinding. CIRP Ann 58(2):663–680
3. Deng ZH, Zhang XH, Liu W, Cao H (2009) A hybrid model using genetic algorithm and neural network for process parameters optimization in NC camshaft grinding. Int J Adv Manuf Technol 45(9–10):859
4. Jackson MJ, Davis CJ, Hitchiner MP, Mills B (2001) High-speed grinding with CBN grinding wheels—applications and future technology. J Mater Process Technol 110(1):78–88
5. Stephenson DJ, Jin T, Corbett J (2002) High efficiency deep grinding of a low alloy steel with plated CBN wheels. CIRP Ann 51(1): 241–244
6. Wu Y, Shen M, Qu M, Xie G, Shang Z, Jin T (2019) An experimental investigation on surface layer damage in high-efficiency and low-damage grinding of rail by slotted CBN grinding wheel. Int J Adv Manuf Technol 105(7–8):2833–2841
7. Malkin S, Guo C (2007) Thermal analysis of grinding. CIRP Ann 56(2):760–782
8. Guo C, Malkin S (1996) Inverse heat transfer analysis of grinding, part 1: methods. J Eng Ind 118(1):137–142
9. Guo C, Malkin S (1996) Inverse heat transfer analysis of grinding, part 2: applications. J Eng Ind 118(1):143–149
10. Rowe WB (2001) Thermal analysis of high efficiency deep grinding. Int J Mach Tools Manuf 41(1):1–19
11. Jiang J, Ge P, Sun S, Wang D, Wang Y, Yang Y (2016) From the microscopic interaction mechanism to the grinding temperature field: an integrated modelling on the grinding process. Int J Mach Tools Manuf 110:27–42
12. Brosse A, Naisson P, Hamdi H, Bergheau JM (2008) Temperature measurement and heat flux characterization in grinding using thermography. J Mater Process Technol 201(1–3):590–595
13. Lefebvre A, Lanzetta F, Lipinski P, Torrance AA (2012) Measurement of grinding temperatures using a foil/workpiece thermocouple. Int J Mach Tools Manuf 58:1–10
14. Pang J, Li B, Liu Y, Wu C (2017) Rayleigh heat flux distribution model investigation and workpiece temperature prediction in the cylindrical grinding. Int J Adv Manuf Technol 89(9–12):3231–3241
15. Yi J, Jin T, Deng Z, Zhou W (2019) Estimation of residual stresses in gear form grinding using finite element analysis and experimental study based on grinding force and heat flux distribution models. Int J Adv Manuf Technol 104(1–4):849–866
16. Anderson D, Warkentin A, Bauer R (2008) Comparison of numerically and analytically predicted contact temperatures in shallow

and deep dry grinding with infrared measurements. Int J Mach Tools Manuf 48(3–4):320–328
17. Rowe WB, Morgan MN, Black SCE, Mills B (1996) A simplified approach to control of thermal damage in grinding. CIRP Ann 45(1):299–302
18. Lan S, Jiao F (2019) Modeling of heat source in grinding zone and numerical simulation for grinding temperature field. Int J Adv Manuf Technol 103(5–8):3077–3086
19. Balaji PS, Yadava V (2013) Three dimensional thermal finite element simulation of electro-discharge diamond surface grinding. Simul Model Pract Theory 35:97–117
20. Li HN, Axinte D (2017) On a stochastically grain-discretised model for 2D/3D temperature mapping prediction in grinding. Int J Mach Tools Manuf 116:60–76
21. Nguyen T, Zhang LC (2011) Realisation of grinding-hardening in workpieces of curved surfaces—part 1: plunge cylindrical grinding. Int J Mach Tools Manuf 51(4):309–319
22. Nguyen T, Liu M, Zhang L, Wu Q, Sun D (2014) An investigation of the grinding-hardening induced by traverse cylindrical grinding. J Manuf Sci Eng 136(5):051008
23. Dražumerič R, Roininen R, Badger J, Krajnik P (2018) Temperature-based method for determination of feed increments in crankshaft grinding. J Mater Process Technol 259:228–234
24. Drazumeric R, Badger J, Krajnik P (2014) Geometric, kinematical and thermal analyses of non-round cylindrical grinding. J Mater Process Technol 214(4):818–827
25. Ding Z, Jiang X, Guo M, Liang SY (2018) Investigation of the grinding temperature and energy partition during cylindrical grinding. Int J Adv Manuf Technol 97(5–8):1767–1778
26. Li B, Zhu D, Pang J, Yang J (2011) Quadratic curve heat flux distribution model in the grinding zone. Int J Adv Manuf Technol 54(9–12):931–940
27. García E, Méresse D, Pombo I, Harmand S, Sánchez JA (2014) Identification of heat partition in grinding related to process parameters, using the inverse heat flux conduction model. Appl Therm Eng 66(1–2):122–130
28. Xu X, Malkin S (2001) Comparison of methods to measure grinding temperatures. J Manuf Sci Eng 123(2):191–195
29. Deng H, Xu Z (2019) Dressing methods of superabrasive grinding wheels: a review. J Manuf Process 45:46–69
30. Dai CW, Ding WF, Zhu YJ, Xu JH, Yu HW (2018) Grinding temperature and power consumption in high speed grinding of Inconel 718 nickel-based superalloy with a vitrified CBN wheel. Precis Eng 52:192–200